Electronic Supplementary Information

Efficient overall water splitting catalyzed by robust FeNi₃N nanoparticles with hollow interiors

Zong Liu,[a] Danye Liu,[b] Linyu Zhao,[a] Jingqi Tian,[a*] Jun Yang[b,c*] and Ligang Feng[a*]

[a] *School of Chemistry and Chemical Engineering, Yangzhou University, Yangzhou 225002, PR China. Email: tianjq@yzu.edu.cn (J Tian*); ligang.feng@yzu.edu.cn; fenglg11@gmail.com (L Feng*); ORCID: 0000-0001-9879-0773 (L. Feng)*

[b] *State Key Laboratory of Multiphase Complex Systems, Institute of Process Engineering, Chinese Academy of Sciences, Beijing 100190, China; University of Chinese Academy of Sciences, Beijing 100049, China. Email: jyang@ipe.ac.cn (J. Yang*)*

[c] *Nanjing IPE Institute of Green Manufacturing Industry, Nanjing 211100, Jiangsu, China*

Experimental Section

Materials

All chemicals used were of analytical grade and used as received. $FeCl_2 \cdot 4H_2O$ and $NiCl_2 \cdot 6H_2O$, CTAB, hydrazine hydrate and KOH are from Aladdin Chemistry Co Ltd. Nafion (5 wt. %) is from Sigma-Aldrich Co. Commercial Pt/C was obtained from Johnson Matthey company. Nafion (5 wt%) and ethanol were purchased from Sigma-Aldrich. Ultrapure water (resistivity $\geq$ 18.2 MΩ cm^{-1}) was used to prepare the solutions.

Catalyst fabrication

Synthesis of FeNi-based catalyst. At room temperature, 4.8 g of $NiCl_2 \cdot 6H_2O$, 2.5 g of $FeCl_2 \cdot 4H_2O$ and 100 mg CTAB were added into 100 mL of H_2O under vigorous stirring for 30 min, using the NH_4OH to adjust pH to ca. 8. Then, 10 mL of hydrazine hydrate and 50 mL of H_2O were slowly dripping under vigorous stirring for 30 min. After 3 h sedimentation, the solids were collected by centrifugation, and the obtained FeNi precursor ($FeNi_3$) was washed by water and ethanol, and then dried at 60 °C for 12 h under vacuum before use. The $FeNi_3$ sample was etched under the air atmosphere at 450 °C for 2 h to obtain the $FeNi_3$ oxide nanoparticles ($FeNi_3$-O).

Preparation of $FeNi_3$N-s and $FeNi_3$N-h catalyst. The bulk phase of the $FeNi_3$N-s sample was prepared via nitridation of the $FeNi_3$ sample at 450 °C for 3 h under the NH_3 atmosphere. The $FeNi_3$N-h was obtained via nitridation of the $FeNi_3$-O sample at 450 °C for 3h under the NH_3 atmosphere. For the nitridation process, the heating rate is 2 °C min^{-1}, and the NH_3 flow rate is 50 mL min^{-1}.

Characterization section

Powder X-ray diffraction (XRD) patterns were recorded on a Bruker D8 Advance Powder X-ray diffractometer using a Cu Kα (λ = 1.5405 Å) radiation source operating at 40 kV and 40 mA, and at a scanning rate of 5 ° min^{-1}. A fine powder sample was ground, then put on the glass slide and pressed to make a flat surface under the glass slide. The morphology is examined with a FEI Sirion-200 scanning electron microscope (SEM) and the energy-dispersive X-ray (EDX) analysis was performed on KEVEX X-ray energy detector. All transmission electron microscopy (TEM) and high-resolution TEM (HRTEM) measurements were conducted on a TECNAI G2 operating at 200 kV. The element mapping analysis and energy-dispersive X-ray detector spectrum (EDX)

images were obtained on a TECNAI G2 transmission electron microscope equipped with an EDXA detector: the microscope was operated at an acceleration voltage of 200 kV. All X-Ray photoelectron spectroscopy (XPS) measurements were carried out on a Kratos XSAM-800 spectrometer with an Al Kα radiation source.

All the electrochemical measurements were performed with a Bio-Logic VSP electrochemical workstation (Bio-Logic Co., France). The OER and HER performance were measured in a three-electrode electrochemical cell. A Hg/HgO electrode was used as the reference electrode placed close to the working electrode via luggin capillary tip, the potential was carefully checked before and after the relevant measurements and a graphite rod was used as the counter electrode. Potentials were referenced to a reversible hydrogen electrode (RHE) by adding a value of (0.098 + 0.0592*pH) V. All potentials were converted and referred to the RHE unless stated otherwise. A glassy carbon electrode (3.0 mm in diameter) was used as the working electrode. The glassy carbon electrode was polished separately by 1 micron and 50-nanometer alumina powder. And then the electrode was cleaning in ultrapure water for several times and dried at room temperature before use. The current density was normalized over the geometric surface area of the electrode (0.07 cm^2). A total electrolyte volume of ~50 mL was used to fill the glass cell. Prior to recording the OER and HER activity of as-preparation catalysts, the catalysts were activated by 50 CV scans along with the potential window of 1–1.5 V and –0.5–0 V in 1 M KOH at a scan rate of 50 mV s^{-1}, respectively. The cyclic voltammetry (CV) experiments for the OER and HER were conducted in 1 M KOH at 25 °C using a working electrode and a scan rate of 5 mV s^{-1} across a potential window of 1.00-1.7 V and –0.4–0 V, respectively. The preparation of the catalyst ink was shown in detail as follows: 5 mg of as-preparation catalysts, 960 μL ethanol and 40 μL of Nafion solution were mixed, and then sonicated for 30 min to make a homogeneous dispersion. The as-preparation catalyst ink was loaded onto the glassy carbon disk electrode by drop-casting as the working electrode with a mass loading of 0.25 mg cm^{-2}.

The electrochemical impedance spectra (EIS) were recorded at the frequency range from 1000 kHz to 10 mHz with 10 points per decade. The amplitude of the sinusoidal potential signal was 5 mV. The obtained curves were analyzed and fitted with ZsimpWin computer program. The dynamical stability was tested by recording 1000 CV cycles by cyclic voltammetry scan from 1.0 to 1.7 V and –0.4–0 V at an accelerated scan rate of 50 mV s^{-1} in 1 M KOH, respectively. After

1000 cycles, the stable polarization curve was recorded for comparison with the initial curve. The steady-state stability was measured during electrolysis at a constant potential in both acid and alkaline media for 30 h by chronoamperometry technique. The overpotential was set at 185 mV and 210 mV for HER and OER for FeNi$_3$N-h electrode in alkaline solution, respectively.

The electrochemical surface area (ECSA) was evaluated in terms of doubler layer capacitance (C_{dl}). The ECSA was estimated by cyclic voltammetry (CV) without Faradaic processes occurred region from 0.925 to 1.125 V in 1 M KOH at scan rate 20, 40, 60, 80, and 100 mV s^{-1}. The C_{dl} was estimated by plotting the $\triangle J = (J_a - J_c)/2$ at 1.025 V vs. RHE against the scan rate. The linear slope is the double layer capacitance C_{dl}. The specific capacitance is evaluated for a flat surface by assuming 40 µF cm^{-2} according to previous literature.[1-4] The electrochemically active surface area was achieved by normalizing the doubler layer capacitance to a standard specific capacitance.

Turnover frequency (TOF) was calculated using the following equation assuming all the catalyst as active species[5, 6]:

$$OER: TOF = \frac{J \times A}{(4 \times F \times n)}$$

$$HER: TOF = \frac{J \times A}{(2 \times F \times n)}$$

where J is the current density at a specific overpotential (A cm^{-2}), A is the geometric area of the work electrode samples, F is the Faraday constant (96485 mol C^{-1}), and n is the total number of moles of all the active metal sites (Fe and Ni metal ions) that were deposited onto the glassy carbon electrode.

A gas-tight electrochemical cell coupling with a gas burette was carried out to verify the faradaic yield of samples. The working electrode was prepared by drop-casting catalyst suspension on the glassy carbon electrode with the surface area of 0.07 cm^{-2}. Reach the benchmark current density of 10 mA cm^{-2} at overpotential (185 mV and 210 mV) was applied on the electrode and the volume of the evolved gas was recorded synchronously. Thus, the faradaic yield was calculated from the ratio of the recorded gas volume to the theoretical gas volume during the charge passed through the electrode[7]:

$$Faradaic\ yield = \frac{V_{experimental}}{V_{theoretical}} = \frac{V_{experimental}}{\frac{1(2)}{4} \times \frac{Q}{F} \times V_m}$$

where Q is the charge passed through the electrode, F is Faraday constant (96485 C mol^{-1}), the number 4 means 4 mole electrons per mole O$_2$, the number 1 (2) means 1 O$_2$ (2 mole H$_2$) mole, V_m is molar volume of gas (24.5 L mol^{-1}, 298 K, 101 KPa).

Raman scattering was performed on a Jasco-Raman spectrometer with excitation by 532 nm laser light. The In situ Raman cell with a total electrolyte volume of ~50 mL and a transparent window at the bottom of 1 mm thickness. The Ni foam was cleaned by hydrochloric acid, ethanol and distilled water, respectively. The catalyst coated Ni foam was used as a working electrode with a mass loading of 0.25 mg cm^{-2}. The cyclic voltammetry experiments for the in situ Raman testing were conducted in 1 M KOH at about 25 °C at a scan rate of 0.5 mV s^{-1}, the potential window was set from -0.4 to 0 V vs. RHE for HER and from 1.00 to 1.65 V vs. RHE for OER, respectively. In situ Raman spectra of FeNi$_3$N-h at overpotentials of 210 mV and 185 mV were recorded for OER and HER vs. reaction time in 1 M KOH, respectively.
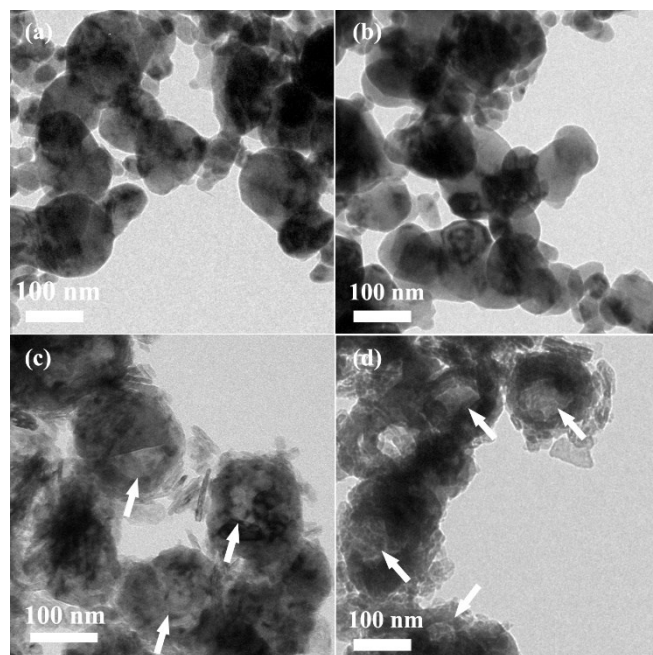
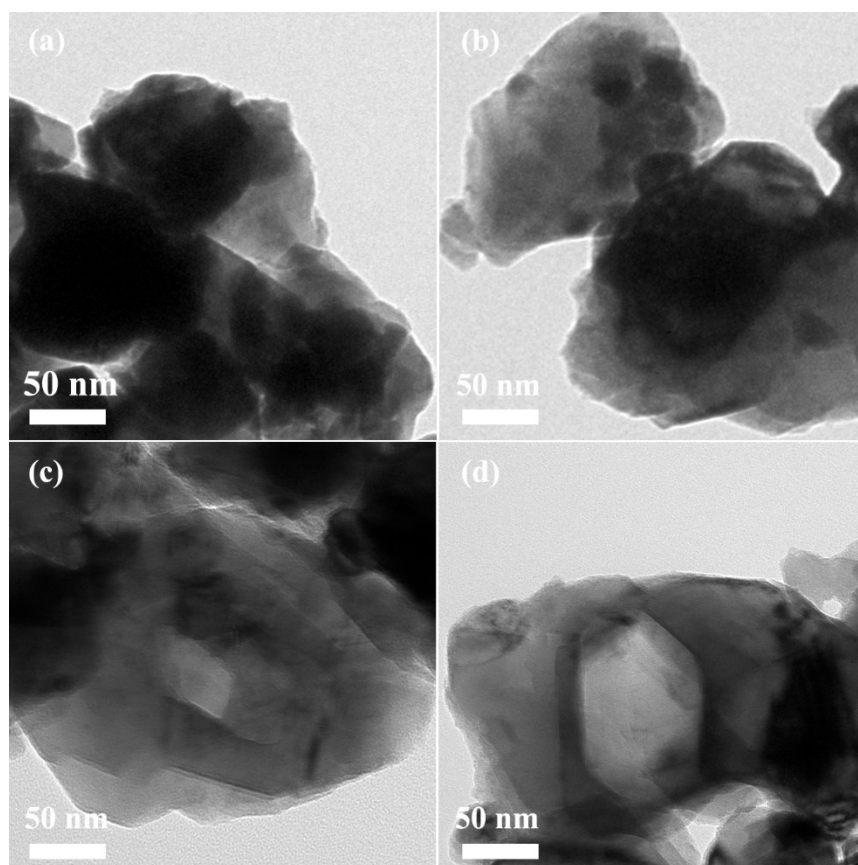**Fig. S1** TEM images of (a,b) FeNi$_3$ and (c,d) FeNi$_3$-O.

Fig. S2 TEM images of (a,b) FeNi$_3$N-s and (c,d) FeNi$_3$N-h.
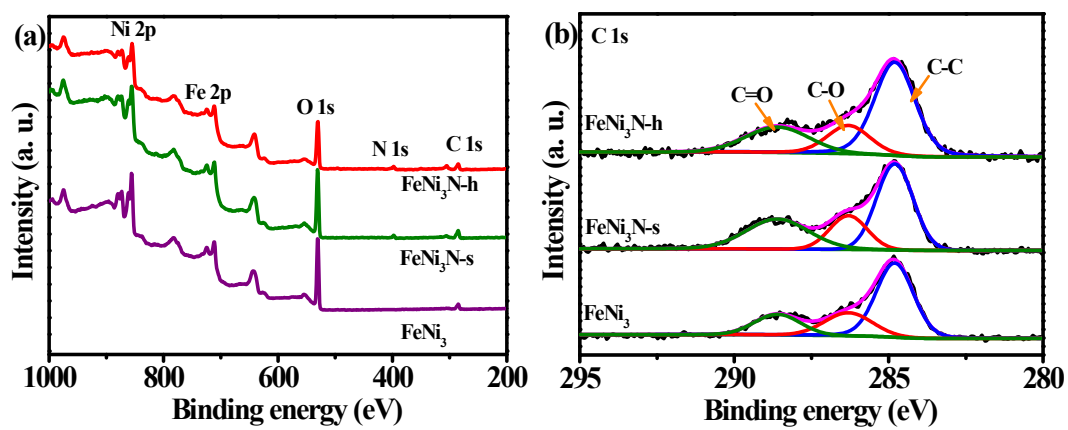
Fig. S3 Full scan XPS spectra of $FeNi_3$, $FeNi_3N$-s and $FeNi_3N$-h (a) and high-resolution C 1s peak of $FeNi_3$, $FeNi_3N$-s and $FeNi_3N$-h (b).
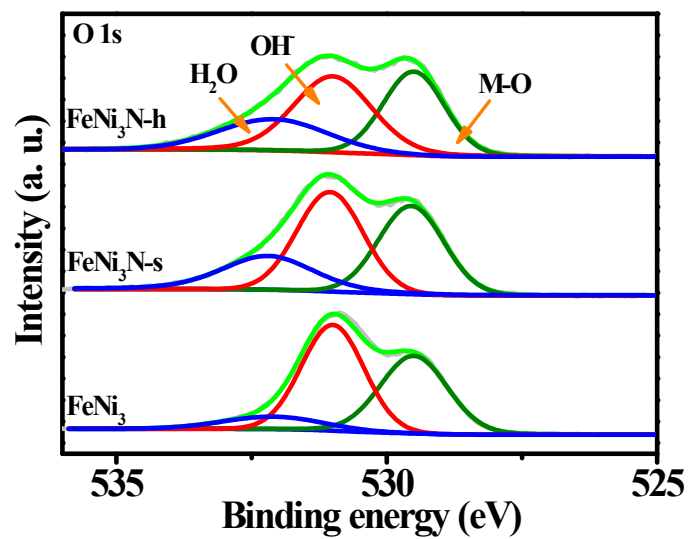
Fig. S4 High-resolution O 1s peak of FeNi$_3$, FeNi$_3$N-s and FeNi$_3$N-h.
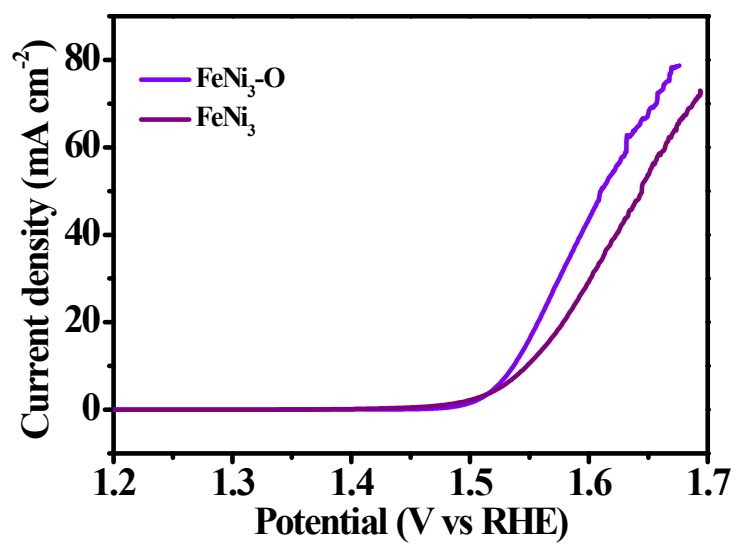
Fig. S5 Polarization curves of FeNi$_3$-O and FeNi$_3$ at a scan rate of 5 mV s^{-1} in 1 M KOH.
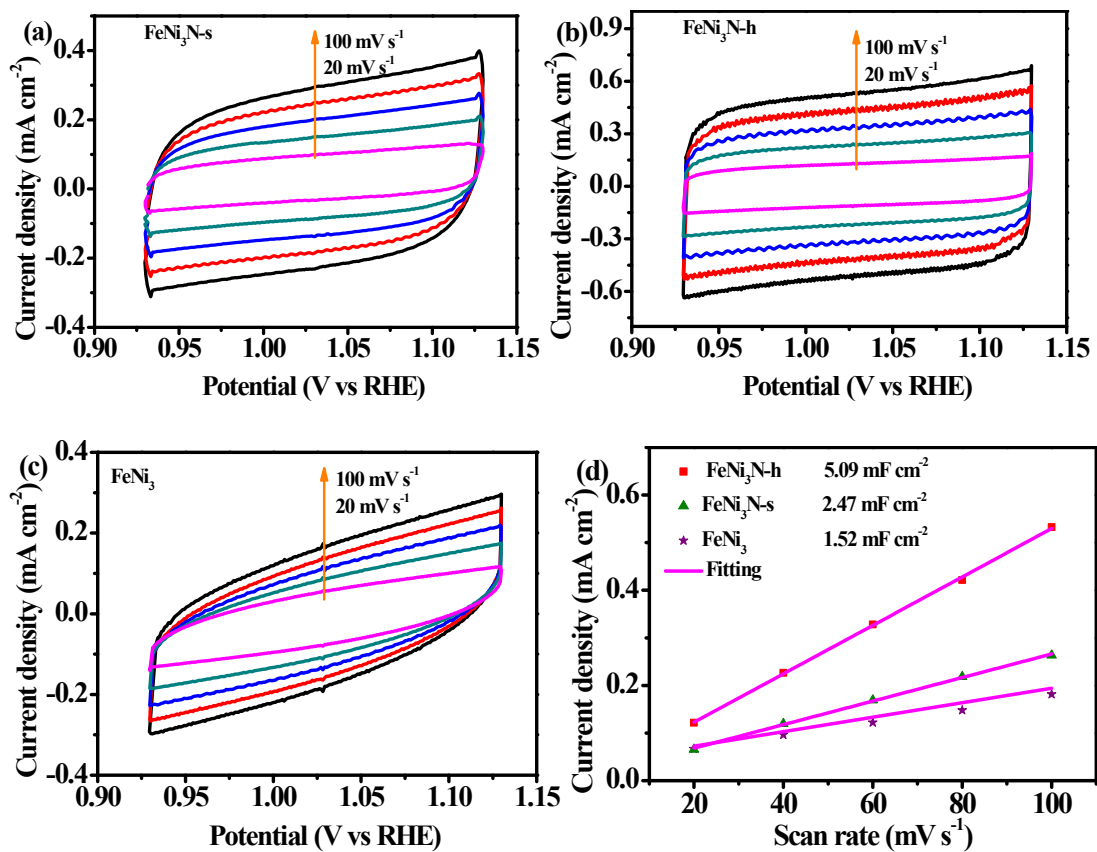
Fig. S6 Cyclic voltammograms of (a) FeNi$_3$N-s, (b) FeNi$_3$N-h and (c) FeNi$_3$ in the non-faradaic capacitance current range from 0.925 V to 1.125 V vs. RHE at scan rates of 20, 40, 60, 80 and 100 mV/s, (d) Current density as a function of the scan rate for the different electrodes.
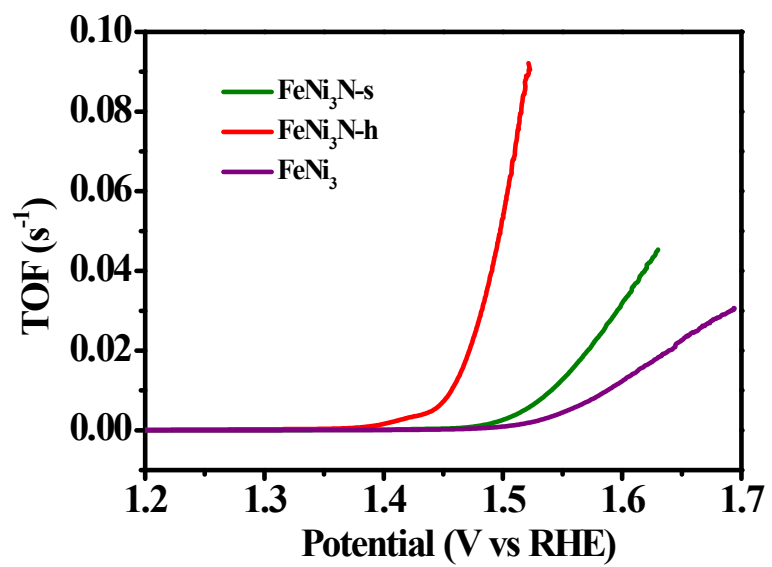
Fig. S7 TOF value of the $FeNi_3$, $FeNi_3N$-h and $FeNi_3N$-s as a function of potentials.
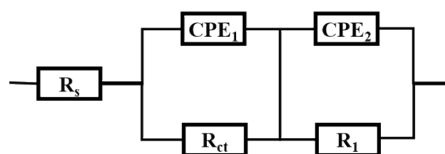
Fig. S8 The equivalent circuit model of EIS analysis of all samples.

The equivalent circuit includes a parallel combination of (R_1, CPE_2) and (R_{ct}, CPE_1) element in series with R_s. The CPE generally was employed to well fit the impedance data by safely treating as an empirical constant without considering the its physical basis. And mostly, it was regarded as the double layer capacitor from the catalyst and catalyst solution. R_s was a sign of the uncompensated solution resistance, R_{ct} was a charge transfer resistance arisen from the relevant electro-chemical oxidation, R_1 was associated to the contact resistance between the catalyst material and the others resistance.
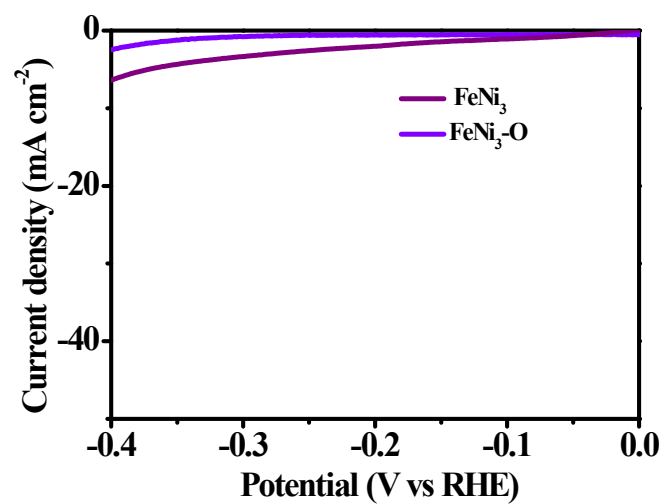
**Fig. S9** Polarization curves of FeNi$_3$-O and FeNi$_3$ at a scan rate of 5 mV s^{-1} in 1 M KOH.
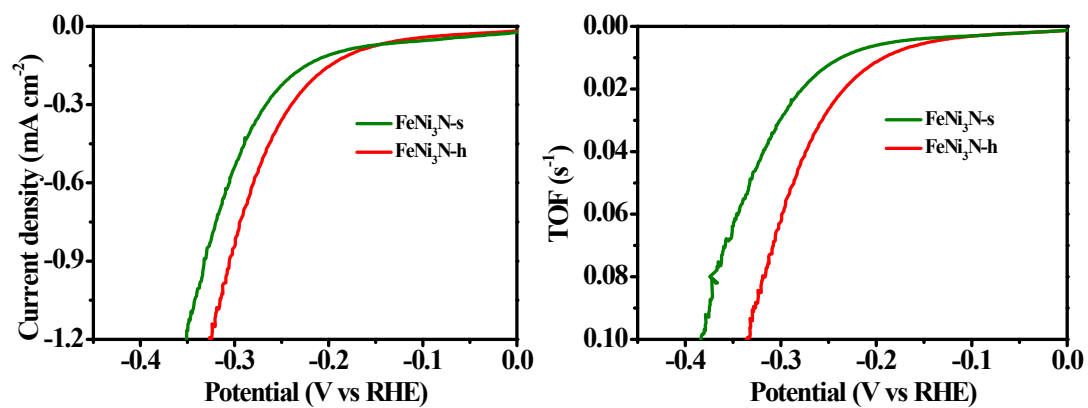
Fig. S10 Specific HER activity of as-prepared catalysts (a). Polarization curves are normalized by the electrochemical active surface areas, which indicates the higher specific activity of the FeNi$_3$N-h and FeNi$_3$N-s. TOF values of the FeNi$_3$N-h and FeNi$_3$N-s as a function of overpotential (b).
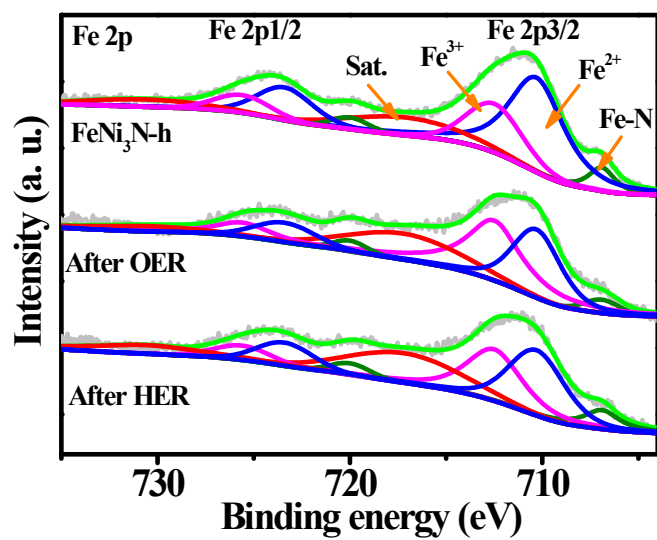
Fig. S11 High-resolution Fe 2p, of FeNi$_3$N-h before and after of OER and HER testing
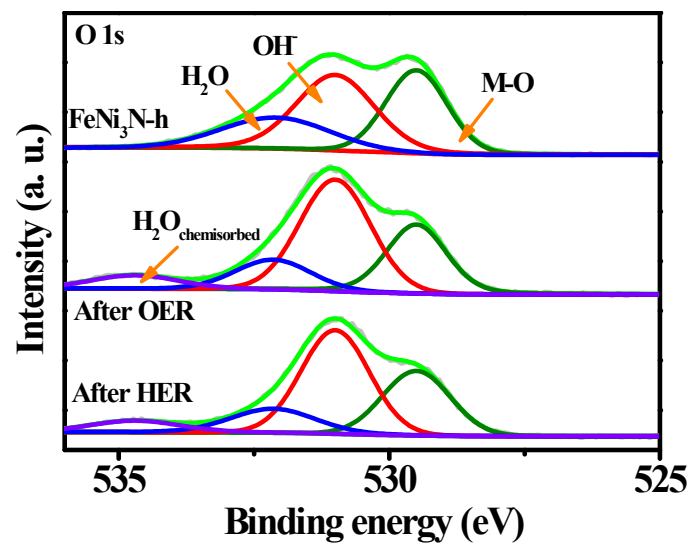
Fig. S12 High-resolution O 1s of FeNi$_3$N-h before and after of OER and HER testing [8].
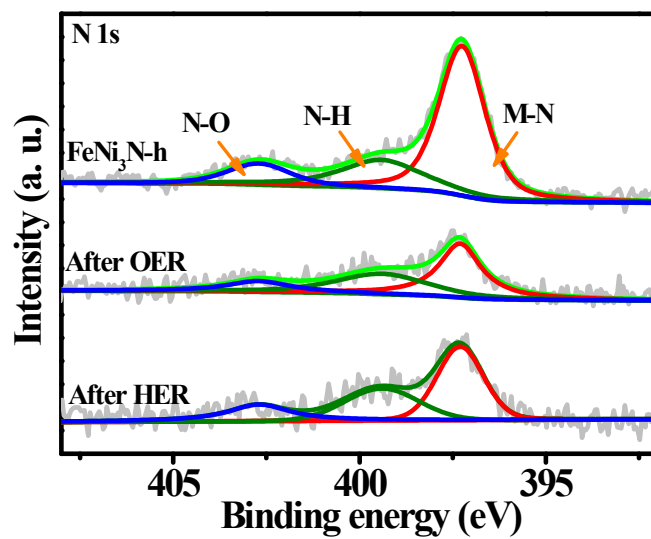
Fig. S13 High-resolution N 1s of FeNi₃N-h before and after of OER and HER testing.

Table S1 The composition of FeNi$_3$N-h derived from EDX spectrum.

Samples	Fe at%	Ni at%	N at%
FeNi$_3$N-h	22.5	69.4	8.1

Note: The C and O elements were not counted because of the influence by the contamination or substrate used for the characterization.

Table S2 The surface composition of $FeNi_3$, $FeNi_3N$-s and $FeNi_3N$-h derived from XPS spectrum.

Samples	Fe 2p at%	Ni 2p at%	N 1s at%
$FeNi_3$	40.0	60.0	NA
$FeNi_3N$-s	35.9	47.6	16.5
$FeNi_3N$-h	38.5	43.9	17.6

Note: The C and O elements were not counted because of the influence by the contamination or substrate used for the characterization.

Table S3 The comparison of some representative OER electrocatalysts with our work in alkaline electrolytes.

Materials	Electrolyte (KOH)	Electrode substrate	Overpotential η_{10} (mV)	Reference
FeNi$_3$N-h	1 M KOH	GCE	210	This work
RuO$_2$	1 M KOH	GCE	315	This work
Ni$_3$Fe/Ni$_3$FeN	1 M KOH	GCE	268	[9]
Ni$_3$FeN/N-G	1 M KOH	GCE	250	[10]
Ni$_3$FeN/r-GO	1 M KOH	GCE	270	[11]
Fe$_2$Ni$_2$N/Co@NCNT	1 M KOH	GCE	280	[12]
Mo-Ni$_3$Fe/Ni$_3$FeN	1 M KOH	GCE	240	[13]
FeNi$_3$N-Ni$_3$S$_2$	1 M KOH	GCE	230	[14]
Fe$_2$Ni$_2$N	1 M KOH	GCE	282	[15]
Ni-Fe-MoN NTs	1 M KOH	GCE	228	[16]
Ni$_3$FeN/Ni	1 M KOH	GCE	200	[17]
Ni$_{1.25}$Ru$_{0.75}$P	1 M KOH	GCE	340	[18]
RuS$_2$-500	1 M KOH	GCE	282	[19]
Ni$_3$FeN	1 M KOH	GCE	280	[20]
RuO$_2$	1 M KOH	GCE	370	[21]
RuO$_2$/Co$_3$O$_4$	1 M KOH	GCE	305	[22]
Ni$_3$FeN/Co,N-CNF	1 M KOH	GCE	270	[23]
Co@Ir/NC-10%	1 M KOH	GCE	280	[24]
IrO$_2$	1 M KOH	GCE	360	[25]
Ru$_2$Ni$_2$ SNs/C	1 M KOH	GCE	310	[26]
2D-NC Fe$_2$Ni$_2$N/rGO NHSs	1 M KOH	GCE	290	[27]
NiMoN-550	1 M KOH	GCE	295	[28]
CoN/Ni$_3$N	1 M KOH	CC	247	[29]
CoxFeyN/graphene	1 M KOH	GCE	266	[30]
Co-NiMoN NRs	1 M KOH	GCE	294	[31]
Ni3FeN-NPs/CC	1 M KOH	CC	241	[32]
Fe-Ni@NC-CNTs	1 M KOH	GCE	274	[33]
Mo-doped Ni$_3$FeN	1 M KOH	NF	250η_{20}	[34]
FeNi-N/CFC	1 M KOH	CC	232η_{20}	[35]
FeNi$_3$N/NG	1 M KOH	GCE	258η_{20}	[36]
FeNi$_3$N/FeNi$_3$	1 M KOH	GCE	254η_{20}	[37]

CC: carbon cloth; NF: Ni foam; GCE: glass carbon electrode

Table S4 EIS fitting parameters from equivalent circuits of samples during OER process.

Samples	R_s / Ω cm^{-2}	R_1 / Ω cm^{-2}	CPE_1 / S s^{-n}	n / 0<n<1	R_{ct} / Ω cm^{-2}	CPE / S s^{-n}	n / 0<n<1
FeNi$_3$N-s	7.8	77.8	1.77E-3	0.81	155.3	1.97E-4	0.81
FeNi$_3$	7.9	200.8	1.57E-4	0.88	197.0	5.66E-4	0.68
FeNi$_3$N-h	7.7	4.0	1.17E-2	0.50	30.0	7.89E-3	0.88

Table S5 The comparison of some representative HER electrocatalysts with our work in alkaline electrolytes.

Materials	Electrolyte (KOH)	Electrode substrate	Overpotential η_{10} (mV)	Reference
FeNi$_3$N-h	1 M KOH	GCE	185	This work
Pt/C	1 M KOH	GCE	65	This work
Co-Ni$_3$N	1 M KOH	GCE	194	[38]
Ni$_3$FeN-Bulk	1 M KOH	GC	208	[20]
Ni$_3$FeN-NPs/CC	1 M KOH	Carbon Cloth	238	[32]
NiCo$_2$N/Ni foam	1 M KOH	Ni foam	290	[39]
CoFeNx HNAs	1 M KOH	Ni foam	200	[40]
Fe$_2$Ni$_2$N	1 M KOH	Ni foam	180	[41]
Ni$_3$FeN-NPs	1 M KOH	GCE	158	[20]
Fe-Ni@NC-CNTs	1 M KOH	GCE	202	[33]
NiCoP NWAs/NF	1 M KOH	Ni foam	197	[42]
NF-Ni$_3$Se$_2$/Ni	1 M KOH	Ni foam	203	[43]

Table S6 EIS fitting parameters from equivalent circuits of samples during HER process.

Samples	R_s / Ω cm^{-2}	R_1 / Ω cm^{-2}	CPE$_1$ / S s^{-n}	n / 0<n<1	R_{ct} / Ω cm^{-2}	CPE / S s^{-n}	n / 0<n<1
FeNi$_3$N-s	7.7	40.4	1.91E-2	0.49	245	7.16E-3	0.92
FeNi$_3$N-h	7.6	26.0	3.13E-2	0.35	150	5.57E-3	0.86
FeNi$_3$	8.0	390	5.74E-2	0.20	2235	2.16E-3	0.68

Table S7 Summary of some reported representative noble metal-based water splitting electrocatalysts

Materials	Electrolyte (KOH)	Electrode substrate	Overall potential V at 10 mA cm^{-2}	Reference
FeNi$_3$N-h‖FeNi$_3$N-h	1 M KOH	GCE	1.63	This work
RuO$_2$‖Pt/C	1 M KOH	GCE	1.62	This work
Fe$_2$Ni$_2$N‖ Fe$_2$Ni$_2$N	1M KOH	NF	1.65	[41]
Co@Ir/NC-10%‖Co@Ir/NC-10%	1 M KOH	GCE	1.667	[24]
Cu@CoFe‖Cu@CoFe	1 M KOH	GCE	1.681	[44]
RuO$_2$/Co$_3$O$_4$‖RuO$_2$/Co$_3$O$_4$	1 M KOH	GCE	1.645	[22]
Rh$_x$P/NPC‖Rh$_x$P/NPC	1 M KOH	GCE	1.64	[45]
Co$_4$N-VN$_{1-x}$O$_x$/CC‖ Co$_4$N-VN$_{1-x}$O$_x$	1 M KOH	CC	1.64	[46]
Ni$_3$FeN-NPs/CC‖Ni$_3$FeN-NPs/CC	1 M KOH	CC	1.81	[32]
NiMo-PVP‖NiFe-PVP	1 M KOH	CF	1.66	[47]
Ni@Mo$_2$C‖Ni@Mo$_2$C	1 M KOH	PC	1.66	[48]
RuO$_2$‖Pt/C	1 M KOH	GCE	1.619	[49]
RuO$_2$‖Pt/C	1 M KOH	CF	1.628	[50]
RuO$_2$‖Pt/C	1 M KOH	NF	1.61	[49]
RuO$_2$‖Pt/C	1 M KOH	CF	1.63	[51]
RuO$_2$‖Pt/C	1 M KOH	CF	1.611	[52]
RuO$_2$‖Pt/C	1 M KOH	CF	1.62	[53]

GCE: glass carbon electrode; NF: Ni foam; PC: porous carbon-supported; CF: Carbon Fibers

Table S8 Analysis of Fe 2p, Ni 2p and N 1s derived from the XPS spectrum before and after HER and OER test.

Catalysts	Fe 2p$_{3/2}$			Ni 2p$_{3/2}$			N 1s		
	Peaks	Binding energy/ eV	ratio	Peaks	Binding energy/ eV	ratio	Peaks	Binding energy/ eV	ratio
FeNi$_3$N-h	Fe-N	706.9	7.7%	Ni-N	852.4	19.6%	M-N	397.3	64.4%
	Fe^{2+}	710.3	64.5%	Ni^{2+}	855.1	80.4%	N-H	399.4	23.9%
	Fe^{3+}	712.5	27.8%	-	-	-	N-O	402.7	11.7%
After HER testing	Fe-N	706.9	4.3%	Ni-N	852.4	10.3%	M-N	397.3	48.1%
	Fe^{2+}	710.3	54.8%	Ni^{2+}	855.6	89.7%	N-H	399.4	31.3%
	Fe^{3+}	712.5	40.9%	-	-	-	N-O	402.7	20.6%
After OER testing	Fe-N	706.9	4.9%	Ni-N	852.4	11.9%	M-N	397.3	49.6%
	Fe^{2+}	710.3	41.9%	Ni^{2+}	855.6	88.1%	N-H	399.4	35.1%
	Fe^{3+}	712.5	53.2%	-	-	-	N-O	402.7	15.3%

Table S9 The surface composition of FeNi$_3$N-h derived from XPS spectrum before and after HER and OER testing, respectively.

Samples	Fe 2p at%	Ni 2p at%	N 1s at%
FeNi$_3$N-h	38.5	43.9	17.6
After HER testing	29.4	60.1	10.5
After OER testing	32.2	56.7	11.1

References

[1] C.C. McCrory, S. Jung, I.M. Ferrer, S.M. Chatman, J.C. Peters, T.F. Jaramillo, Benchmarking hydrogen evolving reaction and oxygen evolving reaction electrocatalysts for solar water splitting devices, J. Am. Chem. Soc., **2015**, *137,* 4347-4357.

[2] C.C.L. McCrory, S. Jung, J.C. Peters, T.F. Jaramillo, Benchmarking Heterogeneous Electrocatalysts for the Oxygen Evolution Reaction, J. Am. Chem. Soc., **2013**, *135,* 16977-16987.

[3] Y. Ruquan, d.A.V. Paz, L. Yuanyue, A.J.M. Josefina, P. Zhiwei, W. Tuo, L. Yilun, Y.B. I., W. Su-Huai, Y.M. Jose, T.J. M., High-Performance Hydrogen Evolution from MoS2(1–x)P x Solid Solution, Adv. Mater., **2016**, *28,* 1427-1432.

[4] G. Dingyi, Q. Jing, Z. Wei, C. Rui, Surface electrochemical modification of a nickel substrate to prepare a NiFe-based electrode for water oxidation, ChemSusChem, **2017**, *10,* 394-400.

[5] L. Trotochaud, J.K. Ranney, K.N. Williams, S.W. Boettcher, Solution-cast metal oxide thin film electrocatalysts for oxygen evolution, J. Am. Chem. Soc., **2012**, *134,* 17253-17261.

[6] J. Jiang, A. Zhang, L. Li, L. Ai, Nickel–cobalt layered double hydroxide nanosheets as high-performance electrocatalyst for oxygen evolution reaction, J. Power Sources, **2015**, *278,* 445-451.

[7] W. Jun, L. Kai, Z. Hai-xia, X. Dan, W. Zhong-li, J. Zheng, W. Zhi-jian, Z. Xin-bo, Synergistic effect between metal–nitrogen–carbon sheets and NiO nanoparticles for enhanced electrochemical water-oxidation performance, Angew. Chem., Int. Ed., **2015**, *54,* 10530-10534.

[8] S. Biniak, G. Szymański, J. Siedlewski, A. Świątkowski, The characterization of activated carbons with oxygen and nitrogen surface groups, Carbon, **1997**, *35,* 1799-1810.

[9] H. Li, S. Ci, M. Zhang, J. Chen, K. Lai, Z. Wen, Facile spray-pyrolysis synthesis of yolk–shell earth-abundant elemental nickel–iron-based nanohybrid electrocatalysts for full water splitting, ChemSusChem, **2017**, *10,* 4756-4763.

[10] S. Zhao, M. Li, M. Han, D. Xu, J. Yang, Y. Lin, N.-E. Shi, Y. Lu, R. Yang, B. Liu, Z. Dai, J. Bao, Defect-rich Ni_3FeN nanocrystals anchored on N-doped graphene for enhanced electrocatalytic oxygen evolution, Adv. Funct. Mater., **2018**, *28,* 1706018.

[11] Y. Gu, S. Chen, J. Ren, Y.A. Jia, C. Chen, S. Komarneni, D. Yang, X. Yao, Electronic structure tuning in Ni_3FeN/r-GO aerogel toward bifunctional electrocatalyst for overall water splitting, ACS nano, **2018**, *12,* 245-253.

[12] M. Wu, G. Zhang, J. Qiao, N. Chen, W. Chen, S. Sun, Ultra-long life rechargeable zinc-air battery based on high-performance trimetallic nitride and NCNT hybrid bifunctional electrocatalysts, Nano Energy, **2019**, *61,* 86-95.

[13] Z. Shao, J. Sun, Z. Yan, K. Huang, F. Tian, H. Xue, Q. Wang, Dual-modulation of phase and electronic structure in hierarchical Ni3Fe/Ni3FeN catalyst by Mo-doping to achieve efficient oxygen evolution reaction, Appl. Surf. Sci., **2020**, *529,* 147172.

[14] S. Liang, M. Jing, E. Pervaiz, H. Guo, T. Thomas, W. Song, J. Xu, A. Saad, J. Wang, H. Shen, J. Liu, M. Yang, Nickel–iron nitride–nickel sulfide composites for oxygen evolution electrocatalysis, ACS Appl. Mater. Interfaces, **2020**, *12,* 41464-41470.

[15] X. Chen, P. Gao, H. Liu, J. Xu, B. Zhang, Y. Zhang, Y. Tang, C. Xiao, In situ growth of iron-nickel nitrides on carbon nanotubes with enhanced stability and activity for oxygen evolution reaction, Electrochim. Acta, **2018**, *267,* 8-14.

[16] C. Zhu, Z. Yin, W. Lai, Y. Sun, L. Liu, X. Zhang, Y. Chen, S.-L. Chou, Fe-Ni-Mo nitride porous nanotubes for full water splitting and Zn-air batteries, Adv. Energy Mater., **2018**, *8,* 1802327.

[17] J. Wang, F. Cao, C. Shen, G. Li, X. Li, X. Yang, S. Li, G. Qin, Nanoscale nickel–iron nitride-derived efficient electrochemical oxygen evolution catalysts, Catal. Sci. Technol., **2020**, *10,* 4458-4466.

[18] D.R. Liyanage, D. Li, Q.B. Cheek, H. Baydoun, S.L. Brock, Synthesis and oxygen evolution reaction (OER) catalytic performance of Ni2−xRuxP nanocrystals: enhancing activity by dilution of the noble metal, J. Mater. Chem. A, **2017**, *5,* 17609-17618.

[19] Y. Zhu, H.A. Tahini, Y. Wang, Q. Lin, Y. Liang, C.M. Doherty, Y. Liu, X. Li, J. Lu, S.C. Smith, C. Selomulya, X. Zhang, Z. Shao, H. Wang, Pyrite-type ruthenium disulfide with tunable disorder and defects enables ultra-efficient overall water splitting, J. Mater. Chem. A, **2019**, *7,* 14222-14232.

[20] X. Jia, Y. Zhao, G. Chen, L. Shang, R. Shi, X. Kang, G.I.N. Waterhouse, L.-Z. Wu, C.-H. Tung, T. Zhang, Ni$_3$FeN nanoparticles derived from ultrathin NiFe-layered double hydroxide nanosheets: An efficient overall water splitting electrocatalyst, Adv. Energy Mater., **2016**, *6,* 1502585.

[21] D. Li, H. Baydoun, B. Kulikowski, S.L. Brock, Boosting the catalytic performance of iron phosphide nanorods for the oxygen evolution reaction by incorporation of manganese, Chem. Mater., **2017**, *29,* 3048-3054.

[22] H. Liu, G. Xia, R. Zhang, P. Jiang, J. Chen, Q. Chen, MOF-derived RuO$_2$/Co$_3$O$_4$ heterojunctions as highly efficient bifunctional electrocatalysts for HER and OER in alkaline solutions, RSC Adv., **2017**, *7,* 3686-3694.

[23] Q. Wang, L. Shang, R. Shi, X. Zhang, G.I.N. Waterhouse, L.-Z. Wu, C.-H. Tung, T. Zhang, 3D carbon nanoframe scaffold-immobilized Ni$_3$FeN nanoparticle electrocatalysts for rechargeable zinc-air batteries' cathodes, Nano Energy, **2017**, *40,* 382-389.

[24] D. Li, Z. Zong, Z. Tang, Z. Liu, S. Chen, Y. Tian, X. Wang, Total water splitting catalyzed by Co@Ir core–shell nanoparticles encapsulated in nitrogen-doped porous carbon derived from metal–organic frameworks, ACS Sustainable Chem. Eng., **2018**, *6,* 5105-5114.

[25] A. Dutta, A.K. Samantara, S.K. Dutta, B.K. Jena, N. Pradhan, Surface-oxidized dicobalt phosphide nanoneedles as a nonprecious, durable, and efficient OER catalyst, ACS Energy Lett., **2016**, *1,* 169-174.

[26] J. Ding, Q. Shao, Y. Feng, X. Huang, Ruthenium-nickel sandwiched nanoplates for efficient water splitting electrocatalysis, Nano Energy, **2018**, *47,* 1-7.

[27] S.H. Kwag, Y.S. Lee, J. Lee, D.I. Jeong, S.B. Kwon, J.H. Yoo, S. Woo, B.S. Lim, W.K. Park, M.-J. Kim, J.H. Kim, B. Lim, B.K. Kang, W.S. Yang, D.H. Yoon, Design of 2D nanocrystalline Fe$_2$Ni$_2$N coated onto graphene nanohybrid sheets for efficient electrocatalytic oxygen evolution, ACS Appl. Energy Mater., **2019**, *2,* 8502-8510.

[28] Z. Yin, Y. Sun, C. Zhu, C. Li, X. Zhang, Y. Chen, Bimetallic Ni–Mo nitride nanotubes as highly active and stable bifunctional electrocatalysts for full water splitting, J. Mater. Chem. A, **2017**, *5,* 13648-13658.

[29] C. Ray, S.C. Lee, B. Jin, A. Kundu, J.H. Park, S. Chan Jun, Conceptual design of three-dimensional CoN/Ni3N-coupled nanograsses integrated on N-doped carbon to serve as efficient and robust water splitting electrocatalysts, J. Mater. Chem. A, **2018**, *6,* 4466-4476.

[30] H. Liu, X. Lu, Y. Hu, R. Chen, P. Zhao, L. Wang, G. Zhu, L. Ma, Z. Jin, Co$_x$Fe$_y$N nanoparticles decorated on graphene sheets as high-performance electrocatalysts for the oxygen evolution reaction, J. Mater. Chem. A, **2019**, *7,* 12489-12497.

[31] Z. Yin, Y. Sun, Y. Jiang, F. Yan, C. Zhu, Y. Chen, Hierarchical Cobalt-doped molybdenum–nickel nitride nanowires as multifunctional electrocatalysts, ACS Appl. Mater. Interfaces, **2019**, *11,* 27751-27759.

[32] Q. Chen, R. Wang, M. Yu, Y. Zeng, F. Lu, X. Kuang, X. Lu, Bifunctional iron–nickel nitride

nanoparticles as flexible and robust electrode for overall water splitting, Electrochim. Acta, **2017**, *247,* 666-673.

[33] X. Zhao, P. Pachfule, S. Li, J.R.J. Simke, J. Schmidt, A. Thomas, Bifunctional electrocatalysts for overall water splitting from an iron/nickel-based bimetallic metal–organic framework/dicyandiamide composite, Angew. Chem. Int. Ed., **2018**, *57,* 8921-8926.

[34] X. Liu, X. Lv, P. Wang, Q. Zhang, B. Huang, Z. Wang, Y. Liu, Z. Zheng, Y. Dai, Improving the HER activity of Ni$_3$FeN to convert the superior OER electrocatalyst to an efficient bifunctional electrocatalyst for overall water splitting by doping with molybdenum, Electrochim. Acta, **2020**, *333,* 135488.

[35] F. Yan, Y. Wang, K. Li, C. Zhu, P. Gao, C. Li, X. Zhang, Y. Chen, Highly stable three-dimensional porous nickel-iron nitride nanosheets for full water splitting at high current densities, Chem. Eur. J., **2017**, *23,* 10187-10194.

[36] L. Liu, F. Yan, K. Li, C. Zhu, Y. Xie, X. Zhang, Y. Chen, Ultrasmall FeNi$_3$N particles with an exposed active (110) surface anchored on nitrogen-doped graphene for multifunctional electrocatalysts, J. Mater. Chem. A, **2019**, *7,* 1083-1091.

[37] X. Fu, J. Zhu, B. Ao, X. Lyu, J. Chen, Enhanced oxygen evolution reaction activity of FeNi$_3$N nanostructures via incorporation of FeNi$_3$, Inorganic Chemistry Communications, **2020**, *113,* 107802.

[38] C. Zhu, A.-L. Wang, W. Xiao, D. Chao, X. Zhang, N.H. Tiep, S. Chen, J. Kang, X. Wang, J. Ding, J. Wang, H. Zhang, H.J. Fan, In situ grown epitaxial heterojunction exhibits high-performance electrocatalytic water splitting, Adv. Mater., **2018**, *30,* 1705516.

[39] Y. Wang, B. Zhang, W. Pan, H. Ma, J. Zhang, 3D porous nickel–cobalt nitrides supported on nickel Foam as efficient electrocatalysts for overall water splitting, ChemSusChem, **2017**, *10,* 4170-4177.

[40] D. Li, Y. Xing, R. Yang, T. Wen, D. Jiang, W. Shi, S. Yuan, Holey cobalt–iron nitride nanosheet arrays as high-performance bifunctional electrocatalysts for overall water splitting, ACS Appl. Mater. Interfaces, **2020**, *12,* 29253-29263.

[41] M. Jiang, Y. Li, Z. Lu, X. Sun, X. Duan, Binary nickel–iron nitride nanoarrays as bifunctional electrocatalysts for overall water splitting, Inorg. Chem. Front., **2016**, *3,* 630-634.

[42] J. Li, G. Wei, Y. Zhu, Y. Xi, X. Pan, Y. Ji, I.V. Zatovsky, W. Han, Hierarchical NiCoP nanocone arrays supported on Ni foam as an efficient and stable bifunctional electrocatalyst for overall water splitting, J. Mater. Chem. A, **2017**, *5,* 14828-14837.

[43] R. Xu, R. Wu, Y. Shi, J. Zhang, B. Zhang, Ni$_3$Se$_2$ nanoforest/Ni foam as a hydrophilic, metallic, and self-supported bifunctional electrocatalyst for both H$_2$ and O$_2$ generations, Nano Energy, **2016**, *24,* 103-110.

[44] L. Yu, H. Zhou, J. Sun, F. Qin, D. Luo, L. Xie, F. Yu, J. Bao, Y. Li, Y. Yu, S. Chen, Z. Ren, Hierarchical Cu@CoFe layered double hydroxide core-shell nanoarchitectures as bifunctional electrocatalysts for efficient overall water splitting, Nano Energy, **2017**, *41,* 327-336.

[45] Q. Qin, H. Jang, L. Chen, G. Nam, X. Liu, J. Cho, Low loading of Rh$_x$P and RuP on N, P codoped carbon as two trifunctional electrocatalysts for the oxygen and hydrogen electrode reactions, Adv. Energy Mater., **2018**, *8,* 1801478.

[46] S. Dutta, A. Indra, Y. Feng, H. Han, T. Song, Promoting electrocatalytic overall water splitting with nanohybrid of transition metal nitride-oxynitride, Appl. Catal., B, **2019**, *241,* 521-527.

[47] Y. Zhang, X. Xia, X. Cao, B. Zhang, N.H. Tiep, H. He, S. Chen, Y. Huang, H.J. Fan, Ultrafine metal nanoparticles/N-doped porous carbon hybrids coated on carbon fibers as flexible and binder-free

water splitting catalysts, Adv. Energy Mater., **2017**, *7,* 1700220.

[48] Z.-Y. Yu, Y. Duan, M.-R. Gao, C.-C. Lang, Y.-R. Zheng, S.-H. Yu, A one-dimensional porous carbon-supported Ni/Mo2C dual catalyst for efficient water splitting, Chem. Sci., **2017**, *8,* 968-973.

[49] T. He, Y. Peng, Q. Li, J.E. Lu, Q. Liu, R. Mercado, Y. Chen, F. Nichols, Y. Zhang, S. Chen, Nanocomposites based on ruthenium nanoparticles supported on cobalt and nitrogen-codoped graphene nanosheets as bifunctional catalysts for electrochemical water splitting, ACS Applied Materials & Interfaces, **2019**, *11,* 46912-46919.

[50] Z. Qian, Y. Chen, Z. Tang, Z. Liu, X. Wang, Y. Tian, W. Gao, Hollow nanocages of $Ni_xCo_{1-x}Se$ for efficient zinc–air batteries and overall water splitting, Nano-Micro Letters, **2019**, *11,* 28.

[51] L. Xia, H. Song, X. Li, X. Zhang, B. Gao, Y. Zheng, K. Huo, P. Chu, Hierarchical 0D−2D Co/Mo selenides as superior bifunctional electrocatalysts for overall water splitting, Frontiers in Chemistry, **2020**, *8,* 382.

[52] C.-Z. Yuan, Y.-F. Jiang, Z.-W. Zhao, S.-J. Zhao, X. Zhou, T.-Y. Cheang, A.-W. Xu, Molecule-assisted synthesis of highly dispersed ultrasmall RuO_2 nanoparticles on nitrogen-doped carbon matrix as ultraefficient bifunctional electrocatalysts for overall water splitting, ACS Sustainable Chem. Eng., **2018**, *6,* 11529-11535.

[53] Q. Jin, B. Ren, D. Li, H. Cui, C. Wang, Plasma-assisted synthesis of self-supporting porous CoNPs@C nanosheet as efficient and stable bifunctional electrocatalysts for overall water splitting, ACS Appl. Mater. Interfaces, **2017**, *9,* 31913-31921.